

Twist engineering of the two-dimensional magnetism in double bilayer chromium triiodide homostructures

Hongchao Xie^{1,+}, Xiangpeng Luo^{1,+}, Gaihua Ye^{2,+}, Zhipeng Ye², Haiwen Ge³, Suk Hyun Sung⁴, Emily Rennich⁵, Shaohua Yan⁶, Yang Fu⁶, Shangjie Tian⁶, Hechang Lei⁶, Robert Hovden⁴, Kai Sun¹, Rui He^{2,*}, & Liuyan Zhao^{1,*}

¹ Department of Physics, University of Michigan, 450 Church Street, Ann Arbor, MI, 48109, USA

² Department of Electrical and Computer Engineering, Texas Tech University, 910 Boston Avenue, Lubbock, TX, 79409, USA

³ Department of Mechanical Engineering, Texas Tech University, 2703 7th Street, Lubbock, TX 79409, USA

⁴ Department of Materials Science and Engineering, University of Michigan, 2300 Hayward Street, Ann Arbor, MI, 48109, USA

⁵ Department of Mechanical Engineering, University of Michigan, 2350 Hayward Street, Ann Arbor, MI, 48109, USA

⁶ Department of Physics and Beijing Key Laboratory of Opto-electronic Functional Materials & Micro-Nano Devices, Renmin University of China, Beijing, 100872, China

* Email: rui.he@ttu.edu; lyzhao@umich.edu

⁺ These authors contributed equally

Twist engineering, or the alignment of two-dimensional (2D) crystalline layers with desired orientations, has led to tremendous success in modulating the charge degree of freedom in hetero- and homo-structures, in particular, in achieving novel correlated and topological electronic phases in moiré electronic crystals^{1,2}. However, although pioneering theoretical efforts have predicted nontrivial magnetism^{3,4} and magnons⁵ out of twisting 2D magnets, experimental realization of twist engineering spin degree of freedom remains elusive. Here, we leverage the archetypal 2D Ising magnet chromium triiodide (CrI₃) to fabricate twisted double bilayer homostructures with tunable twist angles and demonstrate the successful twist engineering of 2D magnetism in them. Using linear and circular polarization-resolved Raman spectroscopy, we identify magneto-Raman signatures of a new magnetic ground state that is sharply distinct from those in natural bilayer (2L) and four-layer (4L) CrI₃. With careful magnetic field and twist angle dependence, we reveal that, for a very small twist angle ($\sim 0.5^\circ$), this emergent magnetism can be well-approximated by a weighted linear superposition of those of 2L and 4L CrI₃ whereas, for a relatively large twist angle ($\sim 5^\circ$), it mostly resembles that of isolated 2L CrI₃. Remarkably, at an intermediate twist angle ($\sim 1.1^\circ$), its magnetism cannot be simply inferred from the 2L and 4L cases, because it lacks sharp spin-flip transitions that are present in 2L and 4L CrI₃ and features a dramatic Raman circular dichroism that is absent in natural 2L and 4L ones. Our results demonstrate the possibility of designing and controlling the spin degree of freedom in 2D magnets using twist engineering.

Moiré superlattice forms when two vertically stacked atomic crystals are rotated with respect to each other, enabling a powerful venue to design and tailor the physical properties of 2D materials, including electronic, phononic, and magnetic ones. So far, it has achieved fruitful results in controlling the charge degree of freedom (DoF) and realizing novel quantum phenomena in both single-particle electronic states and two-particle excitonic states. Outstanding examples include the creation of flat electronic bands^{1,2} that leads to various strongly correlated⁶⁻¹⁰ and topological¹¹⁻¹³ phases for the former case, and the introduction of deep confinement potential that localizes excitonic states to realize moiré excitons^{14,15}, exciton Mott insulators¹⁶, and quantum emitters¹⁷ for the latter. Recently, it has also shown significant impacts on modulating the lattice DoF and induced lattice reconstructions^{18,19}, renormalized phonons²⁰, and moiré phonons²¹. In sharp contrast, the potential and power of moiré superlattices in controlling the spin DoF and engineering the magnetic properties have remained as a pristine area experimentally, despite a few pioneering theoretical predictions including noncollinear magnetism³, topological magnetism⁴, moiré magnon bands⁵, and one-dimensional magnons⁵.

Newly discovered layered magnets have greatly expanded the library of two-dimensional (2D) materials and provided exciting possibilities for the exploration and exploitation of the intrinsic spin DoF at the atomically thin limit²²⁻²⁴. Among the 2D magnetic atomic crystals discovered thus far, atomically thin chromium trihalides, CrX₃ (X = Cl, Br, and I) have attracted extensive interest as an archetype 2D magnet platform for hosting a plethora of novel 2D magnetic phenomena²⁵⁻³¹ and exhibiting versatile tunability with external stimuli³²⁻³⁶. In particular, it has been theoretically calculated³⁷ and experimentally shown^{35,36} in bilayer (2L) CrI₃ that tuning between the monoclinic (AB') and rhombohedral (AB) stacking geometries can lead to magnetic transitions from the layered antiferromagnetic (AFM) to ferromagnetic (FM) order. Such a close relationship between structural stacking symmetries and interlayer magnetism in CrI₃ naturally stimulates the curiosity of investigating the magnetism in CrI₃ moiré magnets where the interlayer exchange coupling is periodically modulated in both sign (i.e., AFM vs FM) and strength (i.e., magnitude).

Here, we fabricate twisted double bilayer (tDB) CrI₃ homostructures with individual 2L CrI₃ to engineer the inter-2L exchange coupling and investigate the resulting moiré magnetism. Our choice of 2L CrI₃ as the building block is based on its significantly narrower structural and magnetic phonon linewidths than those of monolayer CrI₃, suggesting a much better crystalline and magnetic integrity in 2L CrI₃^{38,39}. Figure 1a top panel shows a false-color optical image of a typical tDB CrI₃ sample that was made by tearing a large piece of 2L CrI₃ in the bottom panel into two and then stacking them together at a controlled twist angle of α (see Methods). Electron diffraction (Fig. 1b) shows two sets of 1st and 2nd order Bragg peaks for the two 2L CrI₃ in a tDB CrI₃ sample with the targeted α of 1.0° during fabrication, from which the actual α was

determined to be 0.9° on average with a standard deviation of 0.1° through surveying nine different locations on this sample. The match between targeted and measured values confirms our well control of the twist angle in fabrications, and the small standard deviation suggests the homogeneity of our samples. Dark field transmission electron microscopy (TEM) (Fig. 1c) displays the real-space periodic superstructures with noticeable domain formation. The bright triangles are associated with the strongly coupled regions between two 2L CrI₃ whereas the dark boundaries represent the decoupled boundaries. Similar reconstructing has been observed in low-twist angle graphene bilayers¹⁹ and transition metal dichalcogenide bilayers¹⁸.

Magneto-Raman spectroscopy can capture the interlayer magnetism in few-layer CrI₃, by detecting the unique static magnetism-coupled phonons that break the time-reversal symmetry and have antisymmetric Raman tensors³⁸⁻⁴², in addition to the conventional pure structural phonons. Figure 1d presents representative Raman spectra of tDB CrI₃ with the targeted $\alpha = 1.1^\circ$ in both the crossed and parallel linear polarization channels at 10 K, featuring key Raman modes in three spectral ranges, 75 to 85 cm⁻¹, 95 to 120 cm⁻¹, and 120 to 133 cm⁻¹. These modes are coarsely comparable to those of few-layer CrI₃ among which the Raman modes in the 75 to 85 cm⁻¹ and 120 to 140 cm⁻¹ ranges particularly highlight the contribution from the magnetism-coupled-phonon scattering³⁸. In this work, we focus on the 120 to 133 cm⁻¹ range because the Raman modes here could be related to the moiré magnetism and are of higher intensity than those in 75 to 85 cm⁻¹. Figure 1e zooms into the Raman spectra in the 120 to 133 cm⁻¹ range and includes data in both linearly crossed and parallel channels with incident polarizations at the horizontal and 45° rotated directions, i.e., $\theta_{\text{inc}} = 0^\circ$ and 45° . Clearly, the one primary mode in the parallel channels (U_1^t at 129.4 cm⁻¹) and the three modes in the crossed channels ($U_{2,3,4}^t$ at 129.0 cm⁻¹, 127.4 cm⁻¹, and 126.3 cm⁻¹) all and individually show no polarization dependence, confirming that Raman modes in the crossed (parallel) channels correspond to antisymmetric (fully symmetric) Raman tensors, thus break (preserve) the time-reversal symmetry, and correspond to the static magnetism-coupled (pure structural) phonon contribution, similar to those in natural few-layer CrI₃³⁸. On the other hand, the triplet lineshape of the tDB CrI₃ Raman spectra in the crossed channel shows a clear distinction from those of 2L and 4L CrI₃ with a single (U_2^{2L} at 127.1 cm⁻¹) and two (U_2^{4L} at 128.6 cm⁻¹ and U_4^{4L} at 125.7 cm⁻¹) Raman modes, respectively³⁸, shown in Fig. 2a. Such a distinction strongly suggests the substantial difference in the magnetism between tDB CrI₃ and natural 2L/4L CrI₃.

Having established the Raman signature for the magnetism of tDB CrI₃ and its distinction from those of natural 2L/ 4L CrI₃, we proceed to examine its twist angle dependence. Figure 2a collects Raman spectra over 120 – 133 cm⁻¹ taken on tDB CrI₃ of selected $\alpha = 0.5^\circ$, 1.1° , 2.0° , and 5.0° , as well as 4L and 2L CrI₃, in both the crossed and parallel linear polarization channels at 10 K. We observe that the central mode (U_3^t) in the triplet in the crossed channel increases in intensity and the two modes on its side ($U_{2,4}^t$) decrease as

the twist angle α increases, showing the trend that the magneto-Raman spectra of tDB CrI₃ evolves from resembling most the natural 4L CrI₃ at the lowest α to converging towards the 2L CrI₃ at the highest α . This trend is expected because the inter-2L coupling strength in tDB CrI₃ weakens at larger α , leading to the parallel stacked ($\alpha = 0^\circ$) tDB CrI₃ relaxing to a 4L CrI₃ flake and the large twist angle ones are equivalent to two decoupled 2L CrI₃ films. This intensity evolution is further quantitatively summarized in Fig. 2c where the relative intensity ratio $I_{U_3^t}/(I_{U_2^t} + I_{U_4^t})$ is plotted against α for tDB CrI₃ and compared with those of 4L and 2L CrI₃, showing a monotonous enhancement with increasing α and further confirming the corresponding reduction of inter-2L coupling at larger α . Equally informative is the frequency shift of the Raman modes which is shown in Fig. 2b. At low twist angles (*e.g.*, $\alpha = 0.5^\circ, 1.1^\circ$), the frequencies of U_2^t and U_4^t in tDB CrI₃ match with those of U_2^{4L} and U_4^{4L} in 4L CrI₃, respectively, whereas the frequency of U_3^t is close to that of U_2^{2L} in 2L CrI₃ which appears in the crossed channel (the same as U_3^t) and that of U_3^{4L} in 4L CrI₃ which is however absent in the crossed channel (in contrast to U_3^t). As the twist angle increases, the frequencies of U_2^t and U_4^t blueshift towards their high-frequency neighbors U_1^t and U_3^t . Eventually, at large twist angles (*e.g.*, $\alpha = 5^\circ$), the frequencies of $U_{2,4}^t$ become nearly indistinguishable from $U_{1,3}^t$ and approach those of $U_{1,2}^{2L}$ in 2L CrI₃. The correspondence of mode frequencies between the fabricated tDB CrI₃ and the natural 4L/2L CrI₃ reveals that magnetism-coupled-phonon contributions for U_2^t and U_4^t arise from regions with strong inter-2L coupling, resembling the 4L-like case, whereas that for U_3^t is dominated by the decoupled regions, mimicking the 2L-like case. The twist angle dependencies of mode frequencies and the relative intensity ratio both confirm the reduction of inter-2L coupling and the suppression of strongly coupled 2L-2L regions in tDB CrI₃ at larger α .

Out-of-plane magnetic field (B_\perp) is known to introduce sharp spin-flip transitions in few-layer CrI₃, which is nicely captured in the B_\perp dependence of Raman spectra of the magnetism-coupled phonon scattering³⁸. We now proceed to more in-depth investigations of the engineered magnetism in tDB CrI₃ by performing its magnetic field dependencies for selected twist angles and comparing them across one another and with natural 4L/2L CrI₃. Figures 3a-e present the false color maps of the B_\perp dependent magneto-Raman spectra for 4L CrI₃, tDB CrI₃ at selected twist angles of $\alpha = 0.5^\circ, 1.1^\circ$, and 5.0° , and 2L CrI₃, respectively, in the linearly crossed channel at 10 K, and Figures 3f-j summarize their corresponding B_\perp dependencies of the fitted mode intensities of the magnetism-coupled phonons. We first briefly summarize the evolutions of $U_i^{4L/2L}$, with $i = 1 - 4$ for 4L and $i = 1 - 2$ for 2L CrI₃, upon increasing B_\perp as a reference for understanding those of U_{1-4}^t for tDB CrI₃. For 4L CrI₃, U_1^{4L} and U_3^{4L} emerge abruptly at $B_{c1} = 0.7$ T and then sharply jump upwards and downwards, respectively, at $B_{c2} = 1.6$ T, whereas U_2^{4L} and U_4^{4L} both experience two consecutive steep drops at B_{c1} and B_{c2} , with plateaus of constant intensities outside of B_{c1}

and B_{c2} , for which B_{c1} and B_{c2} correspond to two first-order spin flip transitions for the layered magnetism transiting from $\uparrow\downarrow\uparrow$ (layered AFM) first to $\uparrow\downarrow\uparrow\uparrow$ and then to $\uparrow\uparrow\uparrow\uparrow$ (fully spin polarized FM), respectively²⁵, with \uparrow (\downarrow) for out-of-plane magnetic moment aligning up (down). For 2L CrI_3 , U_1^{2L} appears and U_2^{2L} disappears concurrently at $B_c = 0.7$ T with B_c for the spin flip transition from $\uparrow\downarrow$ to $\uparrow\uparrow$ ²⁵.

We now turn to the magnetic field dependencies of U_{1-4}^t in tDB CrI_3 at very small ($\alpha = 0.5^\circ$) and relatively large ($\alpha = 5^\circ$) twist angles, both of which can be well described by a simple weighted linear superposition of those of 4L and 2L CrI_3 . Similar to the 4L case (Figs. 3a and 3f), the 0.5° tDB CrI_3 features two transitions at $B_{c1} = 0.7$ T and $B_{c2} = 1.6$ T with jumps/drops in U_{1-4}^t mode intensities near B_{c1} and B_{c2} of the same trends as those in 4L CrI_3 and plateaus of constant intensities otherwise (Figs. 3b and 3g). Different from the 4L case, U_3^t of the 0.5° tDB CrI_3 is present even below B_{c1} , and the transitions are slightly broadened. As discussed in Fig. 2, U_2^t and U_4^t only originate from regions with strong coupling between the two bilayers in tDB CrI_3 , whereas U_1^t and U_3^t match in frequency with modes in both coupled and decoupled regions. Thus, the behaviors of U_{1-4}^t in the 0.5° tDB CrI_3 can be well accounted for by a weighted add-up of the B_\perp dependencies of U_{1-4}^{4L} and U_{1-2}^{2L} that correspond to the contributions from the strongly coupled and the decoupled 2L-2L regions, respectively. On the other hand, the 5.0° tDB CrI_3 in Figs. 3d and 3i nearly replicates the 2L CrI_3 results in Figs. 3e and 3j, except a minor remnant in U_3^t above $B_c = 0.7$ T. This observation confirms that the 5.0° tDB CrI_3 is primarily regarded as two decoupled 2L CrI_3 with only a tiny fraction of coupled regions. Therefore, the magnetism for both the 0.5° and 5.0° tDB CrI_3 can be well described by the combinations of those of 4L and 2L CrI_3 , which makes sense because at very low twist angles (*e.g.*, 0.5°), the structure of tDB CrI_3 relaxes to maximize the natural 4L-like regions whereas at large twist angles (*e.g.*, 5.0°), the inter-2L coupling in tDB CrI_3 is so significantly reduced to approach two decoupled 2L CrI_3 , similar to many other van der Waals homo- and hetero-structures.

Interestingly, in stark contrast to the 0.5° and 5.0° tDB CrI_3 , the magnetism in the 1.1° tDB CrI_3 can no longer be understood simply from the combination of 4L and 2L CrI_3 because its B_\perp dependence features two key behaviors that are not at all present in those of 4L and 2L CrI_3 (Figs. 3c and 3h). First, around $B_{c1} \approx 0.6$ T, the intensities of U_2^t and U_4^t show a dramatic spike feature whereas U_3^t exhibits a sharp dip, instead of the step-like jumps in 4L/2L CrI_3 . Second, between B_{c1} and $B_{c2} \approx 1.5$ T, U_1^t increases gradually until the saturation at B_{c2} while U_3^t and U_4^t decrease slowly towards a finite intensity and zero, respectively, rather than the plateaus of constant intensities in 4L/2L CrI_3 . These two clear discrepancies between the magnetic field dependencies of the 1.1° tDB and 4L/2L CrI_3 strongly suggest the emergence of a fundamentally new magnetic phase in the tDB CrI_3 of intermediate twist angles, and therefore the distinction from magnetism in both small and large twist angle tDB CrI_3 .

The anomalous behaviors of the 1.1° tDB CrI₃ above are further supported by the observation of large Raman circular dichroism at 0 T which is absolutely zero in 4L and 2L CrI₃³⁸. Figures 4a and 4b show the raw spectra of the 1.1° tDB CrI₃ taken at 0 T in both the LL and RR channels and their corresponding Lorentzian fitting profiles for individual modes, where LL (RR) refers to the incident and scattered light with left- (right-) handed circular polarizations. Here, we note that we could only resolve three ($U_{1,3,4}^t$) out of the four Raman modes because U_2^t is overwhelmed by the spectrally closest and much stronger U_1^t in the same co-circularly polarized channels. Clearly, U_1^t and U_3^t show substantial differences between the LL and RR channels with opposite relative intensities, whereas U_4^t is almost helicity independent. Figure 4c presents the B_{\perp} dependencies of the fitted intensities of $U_{1,3,4}^t$ in both co-circularly polarized channels, where the field is swept from + 2 T to - 2 T and then back to + 2 T. The two key features highlighted in Fig. 3h, the sharp dip/peak around B_{c1} for U_3^t/U_4^t and the gradual evolution between B_{c1} and B_{c2} for all modes, are nicely reproduced in Fig. 4c. In addition, a third feature noticed is that U_1^t and U_3^t exhibit notable hysteresis loops below B_{c1} , consistent with their substantial Raman circular dichroism even at 0 T.

Let us point out two important facts before establishing the understanding on these three key features in the 1.1° tDB CrI₃. First, recent DFT calculations show that both monoclinic and rhombohedral stackings between layers are structurally favorable with nearly identical elastic energies, yet they correspond to distinct interlayer AFM and FM exchange coupling, respectively³⁷. In a moiré supercell of the 1.1° tDB CrI₃, both monoclinic and rhombohedral stacking regions take up appreciable amount of areas and feature the strong but opposite magnetic coupling across the 2L-2L interface, leading to the competition and frustration of spins at the boundaries between the monoclinic and rhombohedral stacking regions. Second, our polar magneto-Raman geometry is only sensitive to the out-of-plane components of spins. Although our probe and analysis do not directly account for the in-plane components of spins which are likely to develop from the aforementioned frustrations^{3,4}, our results on the out-of-plane magnetic orders in tDB CrI₃, at the same time, are compatible with the presence of in-plane spin components.

Therefore, we propose the following model for the magnetism in the 1.1° tDB CrI₃, where the strongly coupled 2L-2L regions have two types, the monoclinic AFM and the rhombohedral FM inter-2L coupling, and the optimized out-of-plane magnetic order features $\uparrow\downarrow\downarrow$ for the monoclinic regions and $\uparrow\uparrow\downarrow$ for the rhombohedral regions. As shown in Supplemental Information S1, based on parameters obtained from DFT calculations, this spin configuration has the lowest magnetic energy for intermediate twist angles. Because the $\uparrow\uparrow\downarrow$ state generates a net magnetization and contributes an effective out-of-plane magnetic field, which causes the re-orientation of the spins in the outermost layer to require a lower external B_{\perp} in the rhombohedral regions than that in the monoclinic regions, i.e., $B_{c1}^R < B_{c1}^M$ with R(M) denoting the rhombohedral(monoclinic) stacking. Therefore, as a function of B_{\perp} , the magnetic state of the 1.1° tDB CrI₃

undergoes three critical transitions at $B_{c1}^R = 0.5$ T, $B_{c1}^M = 0.7$ T, and $B_{c2} = 1.5$ T, corresponding to the spin reorientation in the outermost layer in the rhombohedral and monoclinic regions, and the interior layer in the monoclinic regions, as depicted in Fig. 4d. We now can understand the three key features in the 1.1° tDB CrI₃. First, the dip/peak around 0.6 T for U_3^t/U_4^t (Figure 3h) in fact corresponds to the narrow field range between B_{c1}^R and B_{c1}^M , where the spin state of $\uparrow\uparrow\uparrow$ in the rhombohedral regions provides the least magnetism-coupled phonon contribution for $U_{3,4}^t$ modes (see Supplemental Information S2). Second, the gradual B_\perp dependencies of all modes between B_{c1}^M and B_{c2} are then due to spin flop towards the B_\perp direction, either by the expansion of the polarized area or by the increase in the out-of-plane components. Third, the Raman circular dichroism of $U_{1,3}^t$ at 0 T is from the interference between the individual pure structural and magnetism-coupled phonon contributions, both of which are present for the $\uparrow\uparrow\downarrow$ state in the rhombohedral regions at 0 T. Thus, the hysteresis of $U_{1,3}^t$ below B_{c1}^R is naturally explained.

In summary, we have successfully engineered the 2D magnetism in tDB CrI₃ that exhibits a clear twist angle dependence. Although different from that of 4L/2L CrI₃, the magnetism in the very small and large twist angle tDB CrI₃ are dominated by the superpositions between 4L- and 2L-like regions, whereas that in the intermediate twist angle features fundamentally new magnetic orders that are absent in 4L/2L CrI₃. Our results open up experimental pathways for engineering and understanding 2D moiré magnetism, among which we highlight two immediate opportunities. One is the exploitation of in-plane spin component sensitive experimental techniques, for example, nonlinear optical spectroscopy⁴³⁻⁴⁵, to develop a comprehensive understanding of moiré magnets where noncollinear spin textures with in-plane components often happen. The other is the exploration of moiré magnets for which the interlayer exchange coupling dominates over the intralayer exchange isotropy in the composing 2D magnets, such as 2D XY-type magnets^{46,47}, so that the periodic moiré interlayer exchange interaction is the leading order magnetic energy scale.

Methods

Growth of CrI₃ single crystals Single crystals of CrI₃ were grown by the chemical vapor transport method. Chromium power (99.99% purity) and iodine flakes (99.999% purity) in a 1:3 molar ratio were put into a silicon tube with a length of 200 mm and an inner diameter of 14 mm. The tube was pumped down to 0.01 Pa and sealed under vacuum, and then placed in a two-zone horizontal tube furnace whose two zones were raised up slowly to 903 K and 823 K for 2 days and then held for another 7 days. Shiny, black, plate-like crystals with lateral dimensions of up to several millimeters were obtained from this growth procedure.

Fabrications of 2D CrI₃ and tDB CrI₃ Atomically thin 2D CrI₃ flakes were exfoliated in a nitrogen-filled glovebox, and their thickness was first determined by the optical color contrast to select natural 4L and 2L CrI₃ and further confirmed using Raman spectroscopy at 10 K. Using a polymer-stamping technique inside the glovebox, large-size (lateral dimensions greater than 10 μm) 2L CrI₃ flakes were torn into two parts with similar sizes, one of which was rotated by a well-controlled rotation micrometer for targeted twist angles and then brought down to stack with the remaining half. Both 4L/2L and tDB CrI₃ samples were sandwiched between two few-layer hBN flakes to avoid surface reactions with oxygen and moisture in the ambient environment after taking out from the glovebox. The samples for magneto-Raman spectroscopy measurements were placed onto the SiO₂/Si substrate, and those for TEM measurements were transferred onto to TEM grids.

Micro-Raman spectroscopy Micro-Raman spectroscopy measurements were carried out using a 632.81 nm excitation laser with a full width half maximum (FWHM) of 0.85 cm⁻¹, on the resonance with the charge transfer and Cr³⁺ + ⁴A₂ to ⁴A₁ transitions of CrI₃ in order to increase the Raman sensitivity. The laser beam on the sample site was focused down to ~ 3 μm FWHM in diameter using a 40× transmissive objective, and the laser power was kept at about 80 μW, in order to minimize the local heating effect during measurements. Backscattering geometry was used, where the scattered light was dispersed by a Horiba LabRAM HR Evolution Raman microscope (1800 grooves/mm grating) from Horiba Scientific and detected by a thermoelectric cooled CCD camera from Horiba Scientific. A commercial variable temperature (< 10 K – 325 K), closed cycle, microscopy cryostat from Cryo Industries of America, Inc was interfaced with the Raman microscope. A commercial cryogen free room-temperature-bore (2'' in diameter and 6.88'' long) superconducting magnet from Cryo Industries of America, Inc was used to achieve the variable out-of-plane magnetic field from 0 T to 2 T. The cryostat cold finger, on which the samples were mounted, was inserted into the center of the room-temperature-bore of the magnet. The linearly polarized magnto-Raman measurements were calibrated by suppressing the Rayleigh line in the linearly crossed channel, so as to overcome the Faraday artifact that is caused by the stray magnetic fields passing through

the objective. The circularly polarized magneto-Raman measurements were not affected by this Faraday effect, and therefore no corrections were applied.

Transmission Electron Microscopy Crystallographic orientations of the two composing 2L CrI₃ flakes in a tDB CrI₃ homostructure were identified by selected area electron diffraction measurements on Thermo Fisher Talos operated at 200 keV, equipped with Gatan OneView camera. Each Bragg peak was fitted with a 2D Gaussian to quantify the twist angle in reciprocal space. A total of nine locations were surveyed for the homostructure to develop a statistical confidence in assigning the twist angle and its standard deviation. Figure 1c was generated by averaging DF-TEM images from three 5th order Bragg peaks, spaced 120° apart to remove anisotropy.

Acknowledgement

L. Zhao acknowledges the support by NSF CAREER Grant No. DMR-174774 and AFOSR YIP Grant No. FA9550-21-1-0065. R. He acknowledges the support by NSF CAREER Grant No. DMR-1760668. K. Sun acknowledges the support by NSF Grant No. NSF-EFMA-1741618. R. Hovden acknowledges the support from W. M. Keck Foundation. This work made use of facilities at Michigan Center for Materials Characterization. H. Lei acknowledges support by the National Key R&D Program of China (Grant No. 2018YFE0202600, 2016YFA0300504), the National Natural Science Foundation of China (No. 11774423, and 11822412), the Beijing Natural Science Foundation (Grant No. Z200005), and the Fundamental Research Funds for the Central Universities and Research Funds of Renmin University of China (RUC) (Grant No. 18XNLG14 and 19XNLG17, 20XNH062).

Author contributions

L. Zhao, H. Xie, and X. Luo conceived the idea and initiated this project; H. Xie fabricated the 4L and 2L CrI₃ and tDB CrI₃ homostructures; H. Xie, X. Luo, G. Ye, Z. Ye, and H. Ge carried out the Raman experiments under the supervision of L. Zhao and R. He; S. H. Sung, E. Rennich, and R. Hovden performed the TEM characterizations; S. Yan, Y. Fu, S. Tian, and H. Lei grew the vdW CrI₃ bulk single crystals; K. Sun performed the theoretical calculations; H. Xie, X. Luo, R. He, and L. Zhao analyzed the data and wrote the manuscript; all authors participated in the discussion of the results.

Figure captions

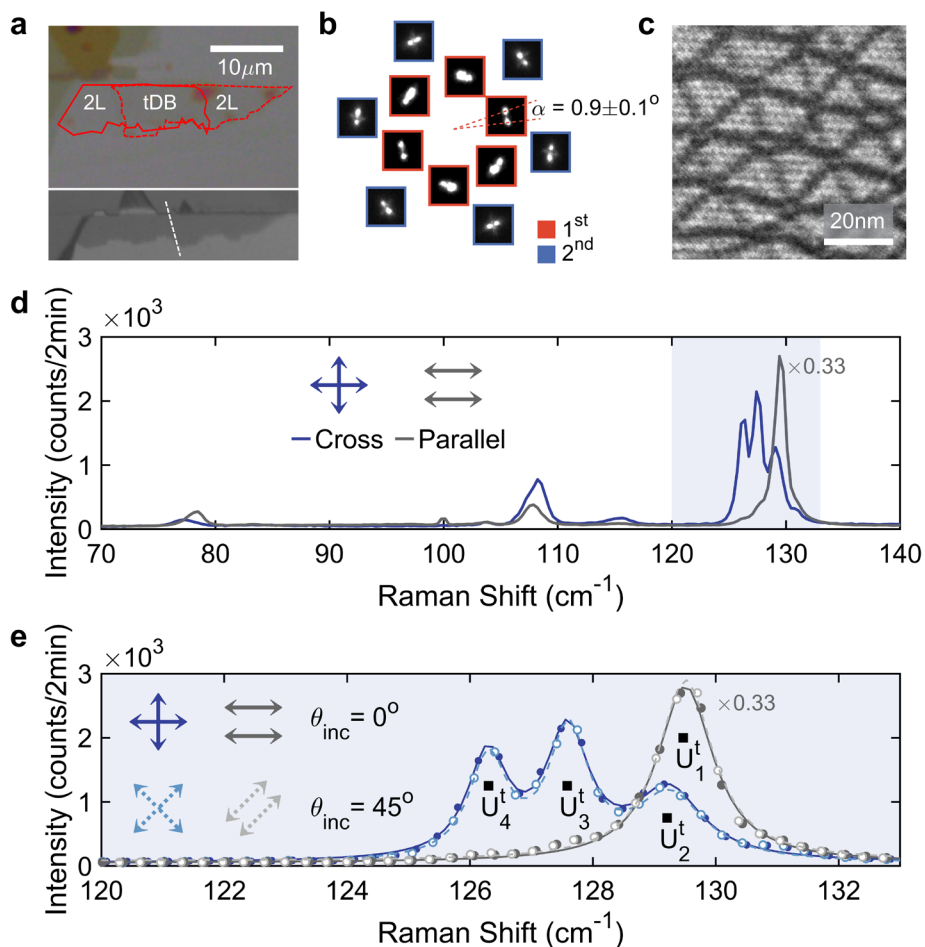


Figure 1. Sample fabrication, TEM and magneto-Raman characterizations of tDB CrI₃. **a.** False-colored optical images for a tDB CrI₃ homostructure (top panel) with two composing 2L CrI₃ outlined with red lines and its original large-size 2L CrI₃ (bottom panel) with the tearing boundary marked with a white dashed line. **b.** Electron diffraction patterns of 1st and 2nd order Bragg peaks for a tDB CrI₃ with a targeted twist angle α of 1.0°, showing the measured value of $\alpha = 0.9 \pm 0.1^\circ$ based on the survey over nine areas in this tDB CrI₃. **c.** Averaged DF-TEM real space image from three 5th order Bragg peaks showing the hexagonal superlattice network in the 0.9° tDB CrI₃ in **b.** **d.** Full-range Raman spectra taken on a 1.1° tDB CrI₃ sample in both the crossed (blue) and parallel (gray) linear polarization channels at 10 K. The parallel channel spectrum is scaled by a factor of 0.33 for a better visual comparison with the crossed channel one. **e.** Zoom-in of Raman spectra over the 120 – 133 cm⁻¹ frequency range taken on the same 1.1° tDB CrI₃ sample as in **d** in both the parallel (blue) and crossed (gray) channels at two incident polarizations of $\theta_{\text{inc}} = 0^\circ$ (filled circles and solid lines) and 45° (open circles and dashed lines) at 10 K. The parallel channel spectra are scaled by a factor of 0.33.

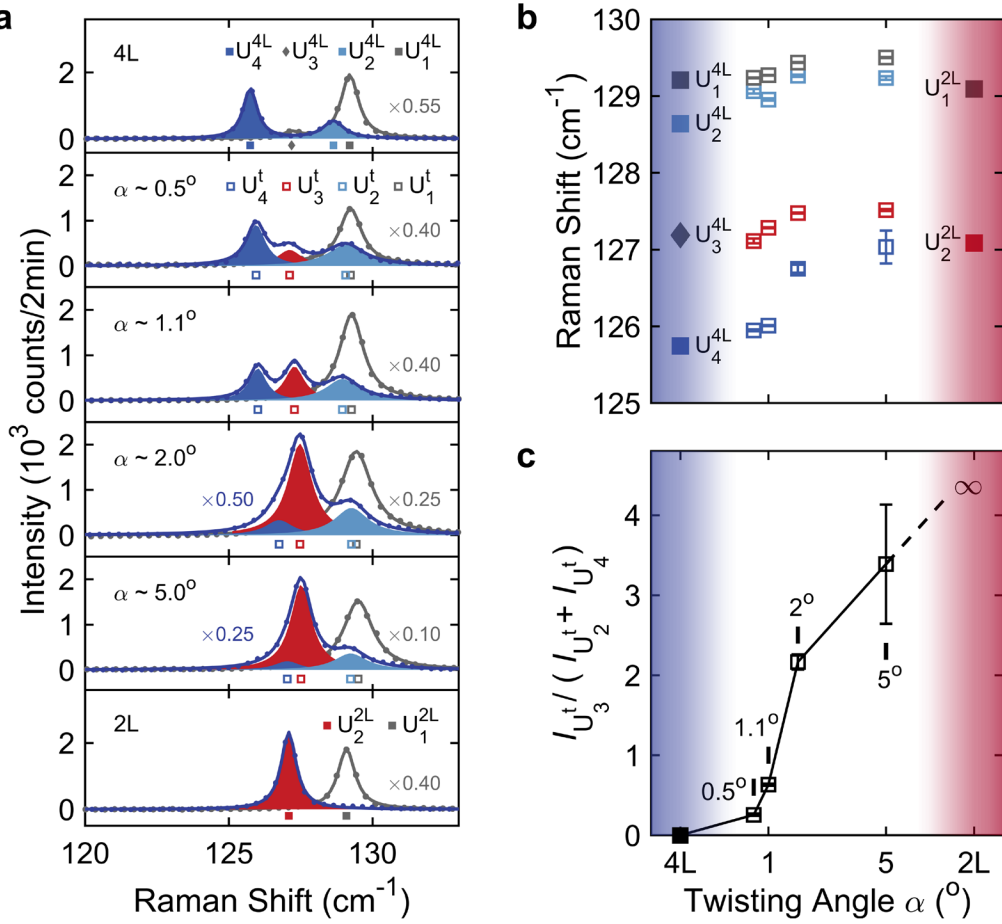


Figure 2. Twist angle dependence of the magneto-Raman spectra of tDB CrI₃. **a.** Raman spectra taken on 4L CrI₃, tDB CrI₃ homostructures with targeted twist angles of $\alpha = 0.5^\circ$, 1.1° , 2.0° , and 5.0° , and 2L CrI₃ in both the crossed (blue dots and lines) and parallel (gray) channels at 10 K. The Raman spectra are scaled by factors labeled in individual panels. The Raman modes are also marked at their corresponding frequencies, with $U_{1,2,3,4}^{4L}$, $U_{1,2,3,4}^t$, and $U_{1,2}^{2L}$ for 4L, tDB, and 2L CrI₃. The colored Lorentzian profiles highlight individual modes appearing in the crossed channel, with red (blue) for the central (two side) mode(s) in the triplet spectra of tDB CrI₃ and the mode(s) of 2L (4L) CrI₃. **b.** Plot of the fitted Raman frequencies of individual modes in every spectrum shown in **a** as a function of the twist angle. **c.** Plot of the intensity ratio $I_{U_3^t} / (I_{U_2^t} + I_{U_4^t})$ as a function of the twist angle. Error bars correspond to one standard error in fitting the Raman spectra.

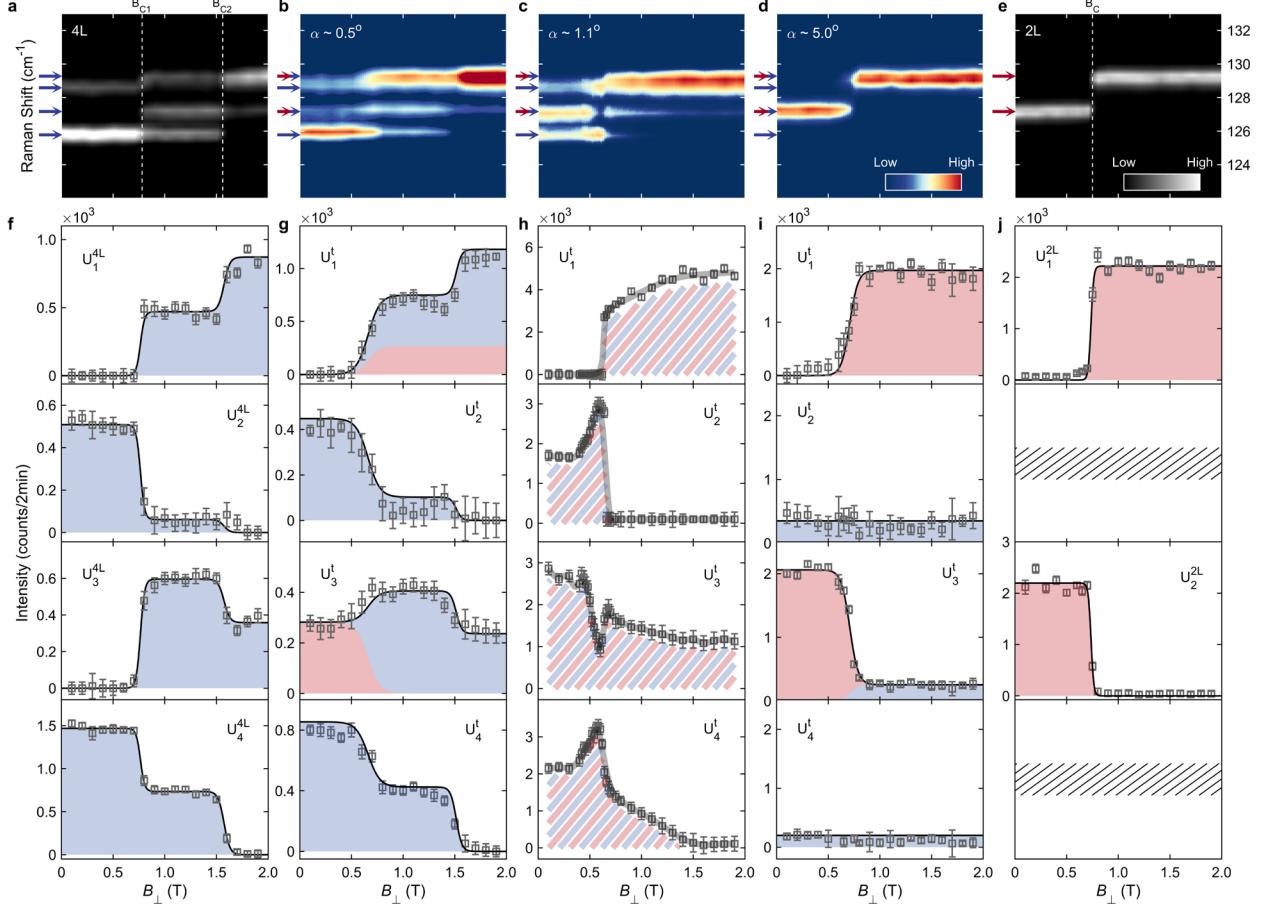


Figure 3. Magnetic field dependence of the magneto-Raman spectra of tDB CrI₃ at selected twist angles. **a-e.** False-colored maps of the B_\perp dependent Raman spectra taken on 4L CrI₃, tDB CrI₃ homostructures with targeted twist angles $\alpha = 0.5^\circ, 1.1^\circ$, and 5.0° , and 2L CrI₃, respectively, in the crossed linear polarization channel at 10 K. The blue arrows mark the frequencies of $U_{1,2,3,4}^{4L}$ for 4L CrI₃, and the red ones are for those of $U_{1,2}^{2L}$ for 2L CrI₃. **f-j.** Plots of the fitted mode intensities as a function of B_\perp for the samples in **a-e**. Open squares are for the fitted values. Thin black lines and solid shaded areas are for the fits to the established model of the magnetism-coupled phonon scattering for the 4L (**f**) and 2L (**j**) CrI₃, and to the proposed weighted linear superpositions of 4L and 2L contributions for the very small (0.5° , **g**) and large (5.0° , **j**) twist angle tDB CrI₃. Thick gray lines and the striped areas in **h** are guide to the eye. Error bars correspond to one standard error in fitting the Raman spectra.

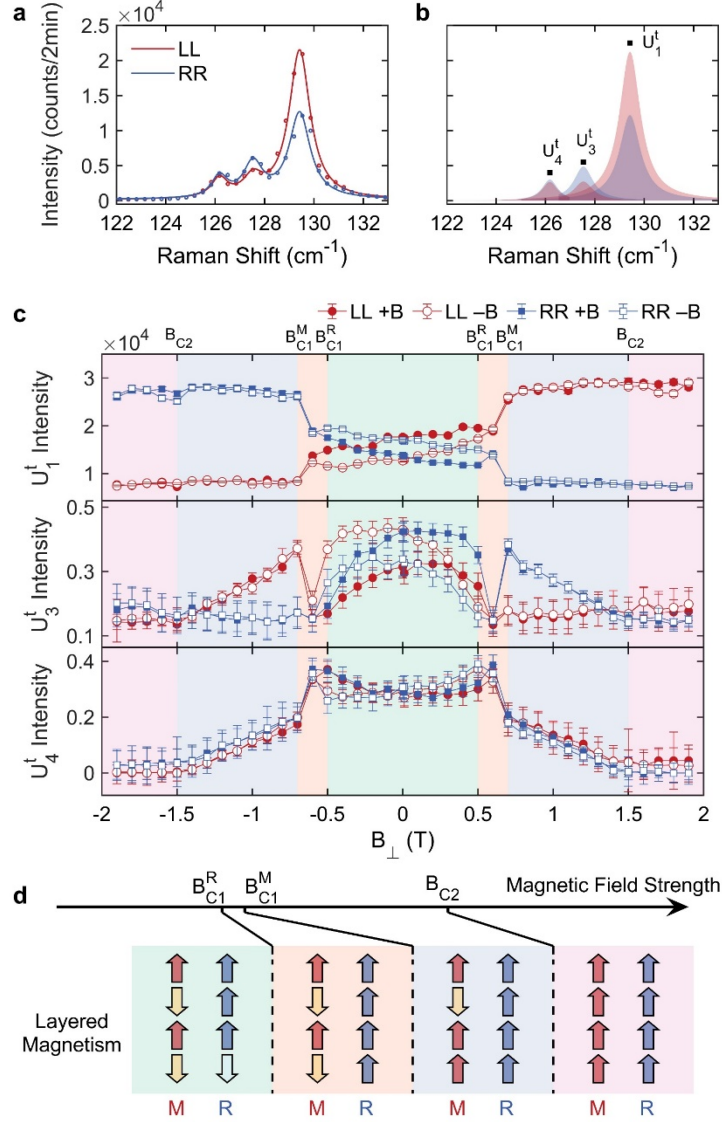


Figure 4. Magnetic circular dichroism for the 1.1° twist angle tDB CrI₃. **a.** Raman spectra taken in the LL (red) and RR (blue) co-circularly polarized channels at 10 K on the 1.1° tDB CrI₃. **b.** Fitted Lorentzian profiles for individual modes (U_{1,3,4}^t) in the Raman spectra in **a.** **c.** Plots of fitted mode intensities for U_{1,3,4}^t as a function of B_⊥ that is swept from + 2 T to - 2 T (decreasing B, open circle/square for the LL/RR channel) and then to + 2 T (increasing B, solid circle/square for the LL/RR channel). Three critical magnetic fields, B_{C1}^R, B_{C1}^M, and B_{C2}, are marked on both the upwards and downwards magnetic fields, and four magnetic field ranges, below B_{C1}^R, B_{C1}^R to B_{C1}^M, B_{C1}^M to B_{C2}, and above B_{C2} are shaded, respectively, with light green, orange, blue, and red. **d.** Sketches of the out-of-plane layered magnetism in the two types of strongly coupled 2L-2L regions of a moiré supercell, monoclinic (M) and rhombohedral (R) ones, evolving as the B_⊥ increases across B_{C1}^R, B_{C1}^M, and B_{C2}.

References

- 1 Balents, L., Dean, C. R., Efetov, D. K. & Young, A. F. Superconductivity and strong correlations in moiré flat bands. *Nature Physics* **16**, 725-733, doi:10.1038/s41567-020-0906-9 (2020).
- 2 Kennes, D. M. *et al.* Moiré heterostructures as a condensed-matter quantum simulator. *Nature Physics* **17**, 155-163, doi:10.1038/s41567-020-01154-3 (2021).
- 3 Hejazi, K., Luo, Z.-X. & Balents, L. Noncollinear phases in moiré magnets. *Proceedings of the National Academy of Sciences* **117**, 10721, doi:10.1073/pnas.2000347117 (2020).
- 4 Tong, Q., Liu, F., Xiao, J. & Yao, W. Skyrmions in the Moiré of van der Waals 2D Magnets. *Nano Letters* **18**, 7194-7199, doi:10.1021/acs.nanolett.8b03315 (2018).
- 5 Wang, C., Gao, Y., Lv, H., Xu, X. & Xiao, D. Stacking Domain Wall Magnons in Twisted van der Waals Magnets. *Physical Review Letters* **125**, 247201, doi:10.1103/PhysRevLett.125.247201 (2020).
- 6 Cao, Y. *et al.* Correlated insulator behaviour at half-filling in magic-angle graphene superlattices. *Nature* **556**, 80-84, doi:10.1038/nature26154 (2018).
- 7 Cao, Y. *et al.* Unconventional superconductivity in magic-angle graphene superlattices. *Nature* **556**, 43-50, doi:10.1038/nature26160 (2018).
- 8 Regan, E. C. *et al.* Mott and generalized Wigner crystal states in WSe₂/WS₂ moiré superlattices. *Nature* **579**, 359-363, doi:10.1038/s41586-020-2092-4 (2020).
- 9 Tang, Y. *et al.* Simulation of Hubbard model physics in WSe₂/WS₂ moiré superlattices. *Nature* **579**, 353-358, doi:10.1038/s41586-020-2085-3 (2020).
- 10 Kim, K. *et al.* Tunable moiré bands and strong correlations in small-twist-angle bilayer graphene. *Proceedings of the National Academy of Sciences* **114**, 3364, doi:10.1073/pnas.1620140114 (2017).
- 11 Nuckolls, K. P. *et al.* Strongly correlated Chern insulators in magic-angle twisted bilayer graphene. *Nature* **588**, 610-615, doi:10.1038/s41586-020-3028-8 (2020).
- 12 Wu, S., Zhang, Z., Watanabe, K., Taniguchi, T. & Andrei, E. Y. Chern insulators, van Hove singularities and topological flat bands in magic-angle twisted bilayer graphene. *Nature Materials*, doi:10.1038/s41563-020-00911-2 (2021).
- 13 Chen, G. *et al.* Tunable correlated Chern insulator and ferromagnetism in a moiré superlattice. *Nature* **579**, 56-61, doi:10.1038/s41586-020-2049-7 (2020).
- 14 Tran, K. *et al.* Evidence for moiré excitons in van der Waals heterostructures. *Nature* **567**, 71-75, doi:10.1038/s41586-019-0975-z (2019).
- 15 Jin, C. *et al.* Observation of moiré excitons in WSe₂/WS₂ heterostructure superlattices. *Nature* **567**, 76-80, doi:10.1038/s41586-019-0976-y (2019).
- 16 Wang, J. *et al.* Optical generation of high carrier densities in 2D semiconductor heterobilayers. *Science Advances* **5**, eaax0145, doi:10.1126/sciadv.aax0145 (2019).
- 17 Seyler, K. L. *et al.* Signatures of moiré-trapped valley excitons in MoSe₂/WSe₂ heterobilayers. *Nature* **567**, 66-70, doi:10.1038/s41586-019-0957-1 (2019).
- 18 Yoo, H. *et al.* Atomic and electronic reconstruction at the van der Waals interface in twisted bilayer graphene. *Nature Materials* **18**, 448-453, doi:10.1038/s41563-019-0346-z (2019).
- 19 Alden, J. S. *et al.* Strain solitons and topological defects in bilayer graphene. *Proceedings of the National Academy of Sciences*, 201309394, doi:10.1073/pnas.1309394110 (2013).
- 20 Quan, J. *et al.* Phonon renormalization in reconstructed MoS₂ moiré superlattices. *Nature Materials*, doi:10.1038/s41563-021-00960-1 (2021).
- 21 Lin, M.-L. *et al.* Moiré Phonons in Twisted Bilayer MoS₂. *ACS Nano* **12**, 8770-8780, doi:10.1021/acs.nano.8b05006 (2018).
- 22 Burch, K. S., Mandrus, D. & Park, J.-G. Magnetism in two-dimensional van der Waals materials. *Nature* **563**, 47-52, doi:10.1038/s41586-018-0631-z (2018).
- 23 Gong, C. & Zhang, X. Two-dimensional magnetic crystals and emergent heterostructure devices. *Science* **363**, eaav4450, doi:10.1126/science.aav4450 (2019).

- 24 Mak, K. F., Shan, J. & Ralph, D. C. Probing and controlling magnetic states in 2D layered magnetic materials. *Nature Reviews Physics* **1**, 646-661, doi:10.1038/s42254-019-0110-y (2019).
- 25 Huang, B. *et al.* Layer-dependent ferromagnetism in a van der Waals crystal down to the monolayer limit. *Nature* **546**, 270-273, doi:10.1038/nature22391 (2017).
- 26 Wang, Z. *et al.* Determining the phase diagram of atomically thin layered antiferromagnet CrCl₃. *Nature Nanotechnology* **14**, 1116-1122, doi:10.1038/s41565-019-0565-0 (2019).
- 27 Chen, W. *et al.* Direct observation of van der Waals stacking-dependent interlayer magnetism. *Science* **366**, 983, doi:10.1126/science.aav1937 (2019).
- 28 Kim, H. H. *et al.* Evolution of interlayer and intralayer magnetism in three atomically thin chromium trihalides. *Proceedings of the National Academy of Sciences* **116**, 11131, doi:10.1073/pnas.1902100116 (2019).
- 29 Klein, D. R. *et al.* Probing magnetism in 2D van der Waals crystalline insulators via electron tunneling. *Science* **360**, 1218, doi:10.1126/science.aar3617 (2018).
- 30 Jin, W. *et al.* Observation of the polaronic character of excitons in a two-dimensional semiconducting magnet CrI₃. *Nature Communications* **11**, 4780, doi:10.1038/s41467-020-18627-x (2020).
- 31 Li, S. *et al.* Magnetic-Field-Induced Quantum Phase Transitions in a van der Waals Magnet. *Physical Review X* **10**, 011075, doi:10.1103/PhysRevX.10.011075 (2020).
- 32 Jiang, S., Li, L., Wang, Z., Mak, K. F. & Shan, J. Controlling magnetism in 2D CrI₃ by electrostatic doping. *Nature Nanotechnology* **13**, 549-553, doi:10.1038/s41565-018-0135-x (2018).
- 33 Huang, B. *et al.* Electrical control of 2D magnetism in bilayer CrI₃. *Nature Nanotechnology* **13**, 544-548, doi:10.1038/s41565-018-0121-3 (2018).
- 34 Jiang, S., Shan, J. & Mak, K. F. Electric-field switching of two-dimensional van der Waals magnets. *Nature Materials* **17**, 406-410, doi:10.1038/s41563-018-0040-6 (2018).
- 35 Li, T. *et al.* Pressure-controlled interlayer magnetism in atomically thin CrI₃. *Nature Materials* **18**, 1303-1308, doi:10.1038/s41563-019-0506-1 (2019).
- 36 Song, T. *et al.* Switching 2D magnetic states via pressure tuning of layer stacking. *Nature Materials* **18**, 1298-1302, doi:10.1038/s41563-019-0505-2 (2019).
- 37 Sivadas, N., Okamoto, S., Xu, X., Fennie, C. J. & Xiao, D. Stacking-Dependent Magnetism in Bilayer CrI₃. *Nano Letters* **18**, 7658-7664, doi:10.1021/acs.nanolett.8b03321 (2018).
- 38 Jin, W. *et al.* Tunable layered-magnetism-assisted magneto-Raman effect in a two-dimensional magnet CrI₃. *Proceedings of the National Academy of Sciences* **117**, 24664, doi:10.1073/pnas.2012980117 (2020).
- 39 Jin, W. *et al.* Raman fingerprint of two terahertz spin wave branches in a two-dimensional honeycomb Ising ferromagnet. *Nature Communications* **9**, 5122, doi:10.1038/s41467-018-07547-6 (2018).
- 40 Huang, B. *et al.* Tuning inelastic light scattering via symmetry control in the two-dimensional magnet CrI₃. *Nature Nanotechnology* **15**, 212-216, doi:10.1038/s41565-019-0598-4 (2020).
- 41 Zhang, Y. *et al.* Magnetic Order-Induced Polarization Anomaly of Raman Scattering in 2D Magnet CrI₃. *Nano Letters* **20**, 729-734, doi:10.1021/acs.nanolett.9b04634 (2020).
- 42 McCreary, A. *et al.* Distinct magneto-Raman signatures of spin-flip phase transitions in CrI₃. *Nature Communications* **11**, 3879, doi:10.1038/s41467-020-17320-3 (2020).
- 43 Zhao, L. *et al.* Evidence of an odd-parity hidden order in a spin-orbit coupled correlated iridate. *Nature Physics* **12**, 32-36, doi:10.1038/nphys3517 (2016).
- 44 Zhao, L. *et al.* A global inversion-symmetry-broken phase inside the pseudogap region of YBa₂Cu₃O_y. *Nature Physics* **13**, 250-254, doi:10.1038/nphys3962 (2017).
- 45 Jin, W. *et al.* Observation of a ferro-rotational order coupled with second-order nonlinear optical fields. *Nature Physics* **16**, 42-46, doi:10.1038/s41567-019-0695-1 (2020).
- 46 Kim, K. *et al.* Suppression of magnetic ordering in XXZ-type antiferromagnetic monolayer NiPS₃. *Nature Communications* **10**, 345, doi:10.1038/s41467-018-08284-6 (2019).

47 Bedoya-Pinto, A. *et al.* Intrinsic 2D-XY ferromagnetism in a van der Waals monolayer. *arXiv preprint arXiv:2006.07605* (2020).

Supplemental Information for

Twist engineering of the two-dimensional magnetism in double bilayer chromium triiodide homostructures

Hongchao Xie^{1,+}, Xiangpeng Luo^{1,+}, Gaihua Ye^{2,+}, Zhipeng Ye², Haiwen Ge³, Suk Hyun Sung⁴, Emily Rennich⁵, Shaohua Yan⁶, Yang Fu⁶, Shangjie Tian⁶, Hechang Lei⁶, Robert Hovden⁴, Kai Sun¹, Rui He^{2,*}, & Liuyan Zhao^{1,*}

¹ Department of Physics, University of Michigan, 450 Church Street, Ann Arbor, MI, 48109, USA

² Department of Electrical and Computer Engineering, Texas Tech University, 910 Boston Avenue, Lubbock, TX, 79409, USA

³ Department of Mechanical Engineering, Texas Tech University, 2703 7th Street, Lubbock, TX 79409, USA

⁴ Department of Materials Science and Engineering, University of Michigan, 2300 Hayward Street, Ann Arbor, MI, 48109, USA

⁵ Department of Mechanical Engineering, University of Michigan, 2350 Hayward Street, Ann Arbor, MI, 48109, USA

⁶ Department of Physics and Beijing Key Laboratory of Opto-electronic Functional Materials & Micro-Nano Devices, Renmin University of China, Beijing, 100872, China

* Email: rui.he@ttu.edu; lyzhao@umich.edu

+ These authors contributed equally

Table of Contents

- S1. Theoretical calculations for determining the out-of-plane magnetic order in tDB CrI₃**
- S2. Calculations of the magnetism-coupled phonon contributions in tDB CrI₃**

S1. Theoretical calculations for determining the out-of-plane magnetic order in tDB CrI₃

Background preparations

Because the polar magneto-Raman geometry (i.e., normal incidence and backscattering geometry with the out-of-plane magnetic field) used in the current experiment, one could only access the out-of-plane components of spins due to the optical selection rule. Therefore, in our model analysis below, we will only focus on the out-of-plane components of spins. In principle, the frustration among spins in moiré magnets could result in spin canting off the out-of-plane direction even in Ising-type magnets¹. While we do not explicitly include possible in-plane components in our model, it is worthwhile pointing out that the main conclusions from the model calculations below are not sensitive to the presence or absence of spin canting off the out-of-plane direction and are compatible with the noncollinear magnetism.

In a moiré superlattice, the periodic modulations of the interlayer stacking geometry lead to the magnetic domain structures in twisted CrI₃². While the structural stacking pattern and the resulting magnetic domain structure are sophisticated, it has been shown theoretically that two types of stacking geometries, AB (i.e., rhombohedral) and AB' (monoclinic) stacking, have the lowest elastic energy³, and therefore, shall be the dominant ones. Instead of trying to capture all microscopic details about the stacking pattern and the lattice reconstruction, in our theory model, we will take a simplified setup and only focus on the most relevant and dominant parts: the monoclinic AB' and the rhombohedral AB stacking, while omitting the other high-energy stacking configurations. In reality, these high-energy stacking area may arise and fill up the regions other than the monoclinic and rhombohedral areas, especially at twist angles greater than $\sim 1.0^\circ$ ². But, the omission of them is sufficient to the leading order approximation.

In the twisted double bilayer (tDB) CrI₃ samples studied in our current work, the interlayer exchange coupling within individual bilayer (2L) CrI₃ remains antiferromagnetic (AFM), just the same as that in regular isolated 2L CrI₃, for which we take the value from the literature, $J_1 = 0.04 \text{ meV}/\mu_B^2$ ^{2,3}. The coupling between the two 2L CrI₃ (i.e., at the interface between the two 2L CrI₃) requires the consideration of two types of structural stacking: monoclinic AB' stacking that corresponds to interlayer AFM exchange coupling and rhombohedral AB stacking that has interlayer ferromagnetic (FM) exchange coupling. We again adopt the values from literature^{2,3}, $J_1 = 0.04 \text{ meV}/\mu_B^2$ for AFM and $J_2 = -0.6 \text{ meV}/\mu_B^2$ for FM. Please note that, according to the first-principles calculations^{2,3}, $|J_2|$ is significantly greater than $|J_1|$. As it will be shown later, this fact is crucial for the development of net magnetization in the tDB CrI₃ with intermediate twist angles. Finally, the intralayer exchange coupling is known to be FM ($J < 0$) and the first-principles calculations give $J = -2.2 \text{ meV}/\mu_B^2$.

Theoretical modeling in tDB CrI₃

For the monoclinic inter-bilayer stacked regions, the interlayer coupling between any two neighboring layers are all AFM with $J_1 = 0.04 \text{ meV}/\mu_B^2$, and therefore its magnetism favors the interlayer AFM order: $\uparrow\downarrow\uparrow$ or $\downarrow\uparrow\downarrow$ from the top to the bottom layer. In contrast, for the rhombohedral inter-bilayer stacked regions, the preferred spin alignment is $\uparrow\downarrow\uparrow$ or $\downarrow\uparrow\downarrow$ because of the FM exchange coupling at the bilayer-bilayer interface. *It is important to note that for both stacking geometries, all these energetically favored spin configurations have zero net magnetization.* In the other word, neither of the stacking favors the development of a net magnetization that is observed in our experiment: *the large Raman circular dichroism for the 1.1° twisted tDB CrI₃ at 0 T.* As we shall see below, to achieve the experimentally observed net

magnetization in 1.1° tDB CrI₃ at 0T, it requires the frustrated spin interactions due to the competition of spins between the monoclinic AFM and the rhombohedral FM regions.

- **the magnetic state with a zero total magnetization**

Case I: One very obvious possible configuration is that the monoclinic region has $\uparrow\downarrow\uparrow\downarrow$ (or the opposite one), whereas the rhombohedral domain has $\uparrow\downarrow\uparrow$ (or the opposite one). In this configuration, each stacking region has its lowest-energy configuration, but the boundaries between them have opposite spin alignments within each of the bottom two layers. The energy penalty associated with such (intralayer) magnetic domain walls is proportional to the length of the domain boundary L multiplied by a factor of 2 because of their presence in two layers and the intralayer FM exchange coupling J , i.e., $E_1 \propto 2JL/a$ where a is the lattice constant of CrI₃. Because the intralayer coupling strength is much greater than the interlayer ones, this energy penalty will become large and dominant, when the domain boundary becomes long.

Case II: If the energy cost for such intralayer domain boundaries becomes too high, the system will favor a different configuration, i.e., avoiding any intralayer magnetic domain boundaries. Take an extreme case example, if the area of the monoclinic domain is much larger than the rhombohedral one, we would expect $\uparrow\downarrow\uparrow\downarrow$ for both monoclinic and rhombohedral stacking regions. This spin configuration does not have any intralayer domain wall penalty, although the rhombohedral one is not in its ground state and is subject to the energy penalty of $E_2 \propto |J_2| (L/a)^2$, where L is the length of the domain boundary and the area shall scale with L^2 .

Depending on the size of the domain L , which is controlled by the twisting angle of tDB CrI₃, the relative ratio between E_1 and E_2 shall change correspondingly. Most importantly, when the domain size is large (small), we shall expect $E_1 \ll E_2$ ($E_1 \gg E_2$), and thus the spin configuration shall follow the first (second) possibilities described above. Here, we emphasize again that all these spin configurations have zero total magnetization.

- **the magnetic state with a non-zero net magnetization**

Case III: For the intermediate domain size, where $E_1 \sim E_2$, new possible spin configuration can arise, for example, $\uparrow\downarrow\uparrow\downarrow$ for the monoclinic region and $\uparrow\uparrow\uparrow\downarrow$ for the rhombohedral region. In this case, the rhombohedral region is not in its ground state, because the top two layers (i.e., the top 2L CrI₃) both have spin up that is in contrast with the interlayer AFM coupling for a 2L CrI₃. This results in an energy penalty of $\sim J_1 (L/a)^2$. At the same time, the intralayer magnetic domain boundary only exists within one layer (i.e., the 2nd layer), which costs an energy of $\sim JL/a$. Therefore, in total, the energy cost for such a spin configuration is $E_3 \propto J_1 (L/a)^2 + JL/a$. Please note that this configuration has only one layer with intralayer magnetic domain wall (in the 2nd layer), so its intralayer energy cost is less than the Case I spin configuration where two layers are subject to intralayer magnetic domain wall (in the 3rd and 4th layers). This is the reason why this Case III configuration is possible to be more energetically favored than the Case I spin arrangement. In comparison to the Case II spin configuration, this Case III configuration has smaller interlayer energy cost, because $J_1 < |J_2|$.

This Case III spin configuration contains both intralayer and interlayer energy penalty (E_3), but the intralayer part is smaller than that of Case I (E_1) and the interlayer one is smaller than that of Case II (E_2). Therefore, when $E_1 \sim E_2$, this configuration could be most energetically favored.

- **the comparison of energies for the three spin configurations**

Below we compare the energies of these three configurations (Case I, II, and III) as a function of the domain size L . Here, we assume that the monoclinic region is greater, because it is the natural stacking for few-layer CrI_3 . Here, we use L to represent the linear size of the rhombohedral stacking region (normalized by the lattice constant a), and L^2 to represent its corresponding area. In reality, it should be multiplied by a geometric factor of order 1, which depends on the shape and other geometrical details of the moiré superlattices, and this factor is set to 1 here for simplicity. At a qualitative level, our conclusion is robust to the exact value of this factor. For a similar argument, we set the length of the magnetic domain boundary to be $4L$.

With this setup and the approximations, we find that the energies of the three spin configurations described above are: $E_1 \approx 8JL$, $E_2 \approx |J_2|L^2$ and $E_3 \approx 4JL + J_1L^2$. The values of J , J_1 and J_2 are obtained from first-principles calculations as mentioned in “background preparation” section ^{2,3}: $J = -2.2 \text{ meV}/\mu_B^2$, $J_1 = 0.04 \text{ meV}/\mu_B^2$, and $J_2 = -0.6 \text{ meV}/\mu_B^2$.

From Fig. S1, we can see that there are two critical lengths, L_1 ($\sim 4J/J_1$) and L_2 as marked, at which the most energetically favored spin configuration alters. Let’s discussion the three regions below, above L_1 , between L_1 and L_2 , and below L_2 .

- (a) Above L_1 when the rhombohedral region dominates over the monoclinic region (i.e., not quite practical – the parameter range where this simple model fails when the twist angle is so big that the inter-bilayer coupling becomes so weak), the most energetically favored spin configuration is Case I: the monoclinic region has $\uparrow\downarrow\uparrow\downarrow$ (or the opposite one) and the rhombohedral domain has $\uparrow\downarrow\uparrow$ (or the opposite one). This gives zero total net magnetization.
- (b) Between L_1 and L_2 when the rhombohedral and monoclinic regions are comparable (i.e., intermediate twist angle), the most energy-saving spin configuration is Case III: the monoclinic region has $\uparrow\downarrow\uparrow\downarrow$ and the rhombohedral domain has $\uparrow\uparrow\downarrow$. This configuration gives a finite total net magnetization, which is consistent with our result in the 1.1° tDB CrI_3 .
- (c) Below L_2 when the monoclinic region dominates over the rhombohedral region (i.e., very small twist angle), the most energetically favored spin configuration is Case II: homogeneous across the monoclinic and rhombohedral regions $\uparrow\downarrow\uparrow\downarrow$. This again gives zero total net magnetization.

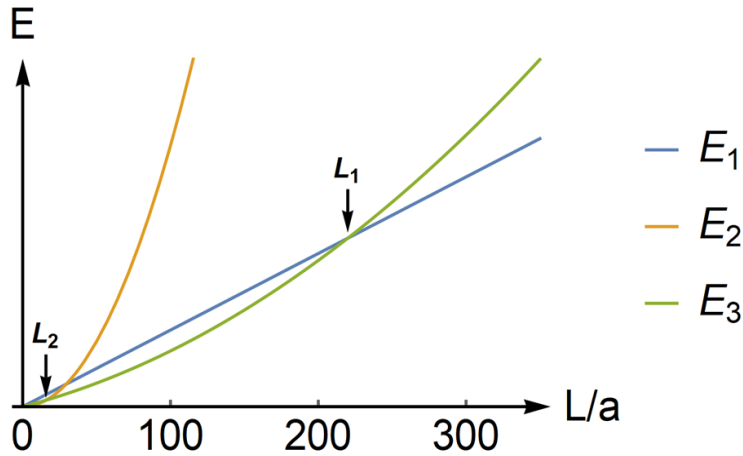


Figure S1 Plots of calculated energy penalty (E_1 , E_2 , and E_3) for the three spin configurations as a function of the rhombohedral stacking region size, normalized to the lattice constant a , i.e., L/a .

- **the consistency between calculations and experiment for the 1.1° tDB CrI₃**

We can do a quantitative comparison between our theoretical calculations and experimental observation. It should be emphasized due to the complicated nature of this material, we made approximations and simplifications in the theory treatment above. In addition, our theory has no fitting parameter at all, and the values of all control parameters are obtained from first-principles calculations. On the other hand, for small energy scales, like interlayer spin exchange, first-principles techniques are limited by resolution and accuracy, which is another source of error for our predicted values. Hence, the theory predicted values here should be treated as an order of magnitude estimation, instead of an exact solution.

With these limitations in mind, here we give key values from the theory predictions. The Case III spin configuration with a net magnetization shall arise at the critical domain size of $L_1 \approx 4J/J_1$. Using values from first-principles calculations^{2,3}, $L \approx 220$. This value is expected to scale with the linear size of a moiré unit cell. For our intermediate angle at which we observed Case III in the experiment, $\theta = 1.1^\circ$, we expect $L \approx 1/\theta \approx 52$, which satisfies the requirement of $L < L_1$ and on the right order of magnitude with L_1 .

Moreover, because the rhombohedral region has net magnetization, under an external magnetic field along (against) the direction of this net magnetization, the magnetic domain for the rhombohedral stacking shall increase (shrink) in size to reduce the energy. This magnetic domain size change is a smooth function of the magnetic field strength, and this is the reason why the signal intensity observed in this phase can vary continuously, gradually as the magnetic field increases.

S2. Calculations of the magnetism-coupled phonon contributions in tDB CrI₃

In few-layer CrI₃, it has been established that the interlayer structural coupling can lead to Davydov splitting of the A_g phonon mode of CrI₃, and these split phonon multiplets have two contributions in the Raman scattering: the pure structural and layered magnetism-coupled phonon contributions that correspond to the fully symmetric and antisymmetric Raman tensors⁴. Here, the layered magnetism-coupled phonon contribution encodes the static magnetic order information and tracks its evolution as a function of external magnetic field.

Here, we exploit the same idea for the strongly coupled 2L-2L regions, including both the monoclinic and rhombohedral inter-2L stacking regions, in tDB CrI₃. We perform the same analysis as in Ref. 4 to compute the magnetism-coupled phonon contributions for the various magnetic orders in the two stacking regions in different magnetic field ranges. The results are summarized in Table. S1 below.

Please note that the atomic displacement eigenvectors are nearly identical for the monoclinic and rhombohedral stacking regions, sharing the same symmetry properties although having slightly different atomic displacement magnitudes across the layers. Therefore, they are listed with the same sketch in Table. S1.

Table S1. Magnetism-phonon coupling strength ($\mathbf{U}_i \cdot \mathbf{M}^{M/R}$) between the phonon mode (\mathbf{U}_i) and the magnetic order ($\mathbf{M}^{M/R}$) in either monoclinic (M in the superscript, red) or rhombohedral (R in the superscript, blue) stacking regions in tDB CrI₃, across all four magnetic field regions with different out-of-plane spin configurations. In each entry, \surd (\times) stands for the presence (absence) of the magnetism-phonon coupling.

Magnetic States	Modes	\mathbf{U}_1^t	\mathbf{U}_2^t	\mathbf{U}_3^t	\mathbf{U}_4^t
	$B_\perp < B_{C1}^R$	$\mathbf{M}^M = \begin{bmatrix} 1 \\ -1 \\ 1 \\ -1 \end{bmatrix}$	\times	\surd	\times
$\mathbf{M}^R = \begin{bmatrix} 1 \\ 1 \\ 1 \\ -1 \end{bmatrix}$		\surd	\surd	\surd	\surd
$B_{C1}^R < B_\perp < B_{C1}^M$	$\mathbf{M}^M = \begin{bmatrix} 1 \\ -1 \\ 1 \\ -1 \end{bmatrix}$	\times	\surd	\times	\surd
	$\mathbf{M}^R = \begin{bmatrix} 1 \\ 1 \\ 1 \\ 1 \end{bmatrix}$	\surd	\times	\times	\times
$B_{C1}^M < B_\perp < B_{C2}$	$\mathbf{M}^M = \begin{bmatrix} 1 \\ -1 \\ 1 \\ 1 \end{bmatrix}$	\surd	\surd	\surd	\surd
	$\mathbf{M}^R = \begin{bmatrix} 1 \\ 1 \\ 1 \\ 1 \end{bmatrix}$	\surd	\times	\times	\times
$B_\perp > B_{C2}$	$\mathbf{M}^M = \begin{bmatrix} 1 \\ 1 \\ 1 \\ 1 \end{bmatrix}$	\surd	\times	\times	\times
	$\mathbf{M}^R = \begin{bmatrix} 1 \\ 1 \\ 1 \\ 1 \end{bmatrix}$	\surd	\times	\times	\times

References

- 1 Hejazi, K., Luo, Z.-X. & Balents, L. Noncollinear phases in moiré magnets. *Proceedings of the National Academy of Sciences* **117**, 10721, doi:10.1073/pnas.2000347117 (2020).
- 2 Wang, C., Gao, Y., Lv, H., Xu, X. & Xiao, D. Stacking Domain Wall Magnons in Twisted van der Waals Magnets. *Physical Review Letters* **125**, 247201, doi:10.1103/PhysRevLett.125.247201 (2020).
- 3 Sivadas, N., Okamoto, S., Xu, X., Fennie, C. J. & Xiao, D. Stacking-Dependent Magnetism in Bilayer CrI₃. *Nano Letters* **18**, 7658-7664, doi:10.1021/acs.nanolett.8b03321 (2018).
- 4 Jin, W. *et al.* Tunable layered-magnetism–assisted magneto-Raman effect in a two-dimensional magnet CrI₃. *Proceedings of the National Academy of Sciences* **117**, 24664, doi:10.1073/pnas.2012980117 (2020).